

A Chiral Switchable Photovoltaic Ferroelectric 1D Perovskite

Yang Hu^{1,#}, Fred Florio^{1,2,#}, Zhizhong Chen¹, W. Adam Phelan³, Maxime A. Siegler³, Zhe Zhou¹, Yuwei Guo¹, Ryan Hawks¹, Jie Jiang^{1,4}, Jing Feng⁴, Lifu Zhang¹, Baiwei Wang¹, Yiping Wang¹, Daniel Gall¹, Edmund F Palermo¹, Zonghuan Lu², Xin Sun², Toh-Ming Lu², Hua Zhou⁵, Yang Ren⁵, Esther Wertz^{2,*}, Ravishankar Sundararaman^{1,2,*}, Jian Shi^{1,6,*}

¹ Department of Materials Science and Engineering, Rensselaer Polytechnic Institute, Troy, NY, 12180

² Department of Physics, Rensselaer Polytechnic Institute, Troy, NY, 12180

³ Department of Chemistry, The Johns Hopkins University, Baltimore, MD 21218

⁴ Faculty of Materials Science and Engineering, Kunming University of Science and Technology Kunming, Yunnan, 650093, China

⁵ X-ray Science Division, Advanced Photon Source, Argonne National Laboratory, Lemont, Argonne, IL 60439, USA.

⁶ Center for Materials, Devices, and Integrated Systems, Rensselaer Polytechnic Institute, Troy, NY, 12180

[#] Equally contributed first authors

^{*}Corresponding authors

A sentence summary: A 1D semiconducting perovskite material shows a hybrid property of chirality and ferroelectricity.

Abstract

Spin and valley degrees of freedom in materials without inversion symmetry exhibit promise for novel device functionality such as spin-valleytronics and circular photogalvanic optoelectronics. The possibility to control the symmetry breaking with electric fields (ferroelectricity) and break additional symmetries including mirror symmetry in one material could enable new physical phenomena where chirality, spin, valley and crystal potential are all strongly coupled together to open up unprecedented device possibilities. In hybrid perovskites, immense flexibility in the structure and chemistry of the organic groups lead to a large design space for achieving such previously unexplored multifunctionality. We report here, a new halide perovskite semiconductor that is simultaneously photo-ferroelectricity switchable and chiral. Infrared and nuclear magnetic resonance spectroscopy, density quantification and single-crystal structural analysis tightly coupled with first-principles calculations determine the material to be a new low-dimensional hybrid perovskite (R)-(-)-1-Cyclohexylethylammonium / (S)-(+)-1-Cyclohexylethylammonium)PbI₃. Optical spectroscopy, electrical, opto-electronic and second-harmonic generation measurements quantify the semiconducting, ferroelectric, switchable pyroelectricity and switchable photo-ferroelectric properties of this material. Single crystal studies of temperature-dependent Synchrotron x-ray diffraction, differential scanning calorimetry, temperature-dependent dielectric constant and temperature-dependent pyroelectricity show a ferroelectric-paraelectric phase transition. Finally, circular dichroism spectroscopy confirms the chirality of this solid-state hybrid perovskite. The unique combination of these properties will facilitate the exploration of new phenomena such as electric field and chiral enantiomer dependent Rashba-Dresselhaus splitting and circular photogalvanic effect.

Introduction

Recently, ferroelectric semiconductors with strong spin-orbit coupling have emerged as theoretically promising candidates for novel electronic functionality such as spin-orbitronics by exploiting electric field-switchable Rashba-Dresselhaus effect (1-6). The capability to break inversion symmetry in a field-dependent manner is the primary source of this phenomenon. Breaking additional symmetries such as chirality in spin-orbit ferroelectric semiconductors would introduce additional perturbations in the Rashba-Dresselhaus physics that could lead to further fine-grained control of the coupled optical, spin, valley and electronic properties of these materials (e.g. chirality-controlled circular photogalvanic effect (7, 8)).

Bringing together spin-orbit-split ferroelectricity and chirality necessitates overcoming two challenges. First, most ferroelectric materials with strong spin-orbit coupling (2-6) either have too low of a band gap for unambiguously achieving ferroelectricity in experiment, resulting in a long-standing debate about whether these materials are even ferroelectric. Second, common chiral materials (9) that exhibit spin-selectivity to photons (10, 11) and electrons (12, 13), such as sodium ammonium tartrate, (S)-alanine and cholesteric liquid crystals, typically have large band gaps with response only in the UV and poor carrier mobilities. Here, we theoretically design and experimentally realize an electrically-switchable, chiral, spin-orbit ferroelectric material in a hybrid lead halide perovskite semiconductor.

Organic-inorganic halide perovskites (14-17) have shown great potential in photovoltaic and electro-optical devices due to their excellent semiconducting properties. The lead-iodine octahedra in hybrid perovskites control the band-edge electronic structure and make them good semiconductors with strong spin-orbit coupling, while the organic groups serve as structural and chemical stabilizers. Importantly, the organic groups provide the flexibility to explore novel functionality, such as ferroelectricity and chirality explored here (Fig. 1), while retaining the desirable semiconducting behavior. Taking such design approach, significant seminar works (18-24) in this field on hybrid perovskite have been inspiring the search of unprecedented materials performance and novel properties. Recently, Xiong et al. reported the two-dimensional ferroelectric perovskite in the form of chiral enantiomers (18). In this report, specifically, by using chiral (R)-(-)-1-Cyclohexylethylamine (R-CYHEA, $C_8H_{15}NH_2$) or (S)-(+)-1-Cyclohexylethylamine (S-CYHEA, $C_8H_{15}NH_2$) for the organic group, we have successfully designed and synthesized a pair of enantiomers R-CYHEAPbI₃ and S-CYHEAPbI₃, which have been found to be chiral and electrically switchable photo ferroelectric perovskite semiconductors. PbI₆ octahedra determine the band structure and transport property, while the organic groups are responsible for chirality and ferroelectricity by removing the material's mirror and inversion symmetry respectively (Fig. 1).

Results and Discussion

We use a solution method to synthesize chiral perovskites from each molecular enantiomer, resulting in needle-like yellow crystals with millimeter dimensions (Fig. 2 **a-b**). Optical images (Fig. 2 **c**) show that the materials from the R-CYHEA and S-CYHEA precursors exhibit similar shapes and colors (in unpolarized light). Nuclear magnetic resonance (NMR) and Fourier-transform infrared spectroscopy (FTIR) confirm the identity of the organic molecule within each crystal, as shown in Fig. 2 **d-e**. Most NMR peaks remain unchanged from the molecule, and a new peak at 7.6 ppm (^1H NMR (500 MHz, DMSO- d_6): δ = 7.60 (s, 3H), 3.00-2.98(m, 1H), 1.72-0.94 (m, 14H)) indicates the incomplete reaction of amino group and HI (Fig. S1). The peaks in FTIR from N-H bonds at around 3200 cm^{-1} are shifted from that in R-CYHEA / S-CYHEA due to the formation of $-\text{NH}_3^+$ from $-\text{NH}_2$ (Fig. S2). Simultaneously, Raman spectroscopy (see Methods) confirms the presence of lead-iodine octahedra with the characteristic peak at around 100 cm^{-1} seen for most lead-iodide perovskites (25, 26), as shown in Fig. S3. (See Methods for further details on the synthesis and spectroscopic measurements.)

X-ray diffraction (XRD) then provides us with detailed structural information, as shown in Fig. S4-S8 and discussed further in Methods. Powder XRD of the materials synthesized from R-CYHEAI and S-CYHEAI are mutually quite similar to each other (Fig. S4-S5), and exhibit none of the peaks of PbI_2 or the molecular precursors. This indicates structural similarity of the two enantiomers and complete transformation from the precursors.

Rietveld refinements and single-crystal XRD measurements (Fig. 2 **g-h**) on the needle-like single crystals at $-173\text{ }^\circ\text{C}$ and $20\text{ }^\circ\text{C}$ (Fig. S9-S11 and tables S1-S3) help determine lattice parameters and atomic positions in greater detail. Existence of a single fast axis in the transmission of linearly-polarized white light (Fig. 2 **f**) and the Kikuchi pattern in our electron backscatter diffraction (EBSD) measurements (Fig. S15) confirm that these needles are indeed single crystals. A combination of XRD crystal determination software, density measurements (Fig. S16) and first-principle calculations (Fig. S17) jointly establish the space group of the crystal to be $P2_1$ with angle $\beta = 89.5121^\circ$ (see more discussions on Table S1-S3 and Fig. S11). Fig. 2 **g** shows the single crystal diffraction pattern of the crystal and Fig. 2 **h** presents the corresponding digitally reconstructed precession photograph. Based on first-principle calculations and single crystal XRD at low temperature and room temperature, we find the lattice expands slightly from $a = 8.612\text{ \AA}$, $b = 7.954\text{ \AA}$, $c = 21.719\text{ \AA}$ at $-173\text{ }^\circ\text{C}$ to $a = 8.628\text{ \AA}$, $b = 8.211\text{ \AA}$, $c = 22.994\text{ \AA}$ at room temperature, with the angle and space group remaining unchanged. The structure and density identify the stoichiometry of the synthesized materials to be R/S-CYHEAPbI₃ (Fig. 2 **i**). First-principles density-functional theory (DFT) calculations fill in the finer structural details beyond XRD

resolution. These calculations show that opposite rotation of the amine groups on either side of the [001] plane, breaks inversion symmetry along the *b*-direction giving rise to polarization in the structure (Fig. S17).

We then investigate the semiconducting property with optical and opto-electronic measurements. Photoluminescence spectroscopy (PL) measurements from a 405 nm excitation laser reveal a weak white PL (Fig. S18), attributed to the Stokes process in low-dimensional halide perovskites (27-29), with response persisting to longer wavelengths including 635 nm, as shown in Fig. S21-S22. A strong absorption transition ranging from ~360 to 410 nm indicates excitonic behavior (Fig. S19-S20) (30), once again consistent with the low-dimensional structure of the crystals (Fig. 2 i).

Next, to test ferroelectricity in our material, we performed temperature-dependent second-harmonic generation (TD-SHG) to analyze this phase transition (Fig. 3 a). The SHG signal decreases dramatically (by half in intensity) at around 85 °C, indicating a phase transition (at 100 °C, the phase transition is complete) from a low-temperature SHG active structure to a high temperature structure which shows no or much weaker SHG signal under our experiment condition. Fig. S23 presents the SHG spectrum from the R symmetry crystal. Additionally, we employed the double-wave technique (31-33) to characterize the polarization-electric field (PE) loops, as shown in Fig. 3 b, clearly indicating the synthesized crystal to be ferroelectric (Fig. S24). The polarization of around 0.03 $\mu\text{C}/\text{cm}^2$ is small compared to commercial ferroelectric materials, due to a combination of a low intrinsic DFT-predicted polarization (see more discussion in Fig. S17 and the associated description) and lack of alignment between the polarization and measurement axes (DFT predicts *b*-axis, Fig. S17). Orientation dependence of the polarization is further confirmed by direction-dependent PE loops in Fig. S26. Further study shows that the polarization reaches 1.2 $\mu\text{C}/\text{cm}^2$ for single crystal sample which will be discussed later.

Having established that our material is both ferroelectric and semiconducting, we measure the typical switchable diode effect (34-37) shown in Fig. 3 c. The photo response of our devices was measured without external bias, and we found that the direction of photo current is dependent on the previous poling process (history of applied electric fields). Specifically, we find a negative photocurrent at 0 V after applying 10 V on the device for 200 s, and a positive photocurrent at 0 V if we applied -10 V instead. This arises from the switching of the ferroelectric, as shown in Fig. 3 d. The polarization results in electric fields that result in opposite directions of band bending at each junction of the semiconductor with the contacts. Specifically, a positive (towards right) bias results in a diode with forward direction towards the right, leading to a negative photo current at zero bias. The negative bias reverses each of these directions. See Fig. S29-S30 for additional measurements and analysis on the absence of ion migration-induced switchable photo response (38). Both transport measurement-

based ferroelectric PE loop and electrically field-switchable photovoltaic ferroelectricity demonstrated here, to our best knowledge, have not been revealed in other chiral perovskites yet (18).

To better understand the band structure of our material, we performed density-functional theory calculations. Fig. 3 e shows the resulting HSE06 band structures for the stable chiral structure XPbI_3 determined using XRD in addition to an alternate X_2PbI_4 structure that is stable for other closely related halide perovskites, such as the non-chiral counterpart shown in panels (ii) and (iv). The predicted band gap for the XPbI_3 structure is 3.70 eV, in good agreement with the experimental absorbance curves shown in Fig. S20. Note that the band gaps switch from direct in the X_2PbI_4 form to indirect in the XPbI_3 form for both the chiral and non-chiral materials. (Analogous band structures calculated using the Perdew-Burke-Ernzerhof (39) are included in Fig. S17, which are very similar in shape but with band gaps smaller by approximately 1 eV.)

Ferroelectric properties are further probed by phase transition study on single crystal sample and device. Temperature dependent synchrotron X-ray diffraction on single crystal sample was performed to check the phase transition seen in our TD-SHG result. As is shown in Fig. 4 a, at around 100 °C, intensity of peak (021) decreases dramatically, which indicates a phase transition. More detailed results are given in our supporting info (SI) Fig. S12-S14 and supplementary videos 1-2. The space group after phase transition can only be determined to be $P2_12_12_1$ based on our XRD result (detailed analysis can be found in Fig. S12-14) and pyroelectric study of single crystal devices presented later. Hence, this phase transition is a ferroelectric to non-ferroelectric one with a Curie temperature of around 100 °C. A differential scanning calorimetry (DSC) test on single crystal sample was performed as another proof of phase transition. As is shown in Fig. 4 b, sudden increase and decrease in the DSC curves show up at around 100 °C, indicating a phase transition. Temperature dependence of real part of dielectric constant on single crystal device is also performed (Fig. 4 c). A peak shows up at around 100 °C, which should also arise from phase transition.

Parasitic capacitance/current dominates under high voltages when our device does not follow a parallel capacitor configuration due to the 1D nature of our material. Hence, conventional P-E loop measurement methods (such as Sawyer-Tower and Double wave) would not be able to reveal the intrinsic property of such 1D material/device. Instead, we have conducted pyroelectric test to probe the ferroelectric properties indirectly (40). Switchable pyrocurrent was obtained (as is shown in Fig. S27), which is consistent with the properties of ferroelectric material. Temperature dependence of pyroelectric current was measured, as is shown in Fig. 4 d. This curve shows a peak at around 100 °C, which indicates a phase transition, and fits well with theoretical calculation based on Landau theory (see SI Fig. S27 for details). Based on this, higher temperature phase is non-ferroelectric, as we saw no pyroelectric current after phase transition. The polarization

at room temperature is around $1.2 \mu\text{C}/\text{cm}^2$ obtained by integration of pyroelectric current. As a substitution of P-E loop, we also measured pyroelectric coefficient versus poling electric field (40). As is shown in Fig. 4 e, a hysteresis loop is observed, which indicates a ferroelectric performance.

Finally, we use circular dichroism (CD) spectroscopy (see Methods) to confirm the chirality of the materials as shown in Fig. 5 a. CD measures the difference in the absorption of left and right circular polarized light (LCP and RCP), as shown in Fig. S32 (18, 41-43). Fig. 5 b, shows that R-CYHEAPbI₃ and S-CYHEAPbI₃ have opposite CD signals at same position, confirming them to be a pair of enantiomers. The maximum CD signal intensity (190 nm to 600 nm) of our perovskite far exceeds that of many common chiral materials, as shown in Fig. 5 c. The intensity of CD signal can be described in the following equation (44, 45):

$$\frac{3K\hbar c}{16\pi^2 N_A} \int \frac{\Delta\epsilon d\lambda}{\beta\lambda} = \text{Im} \left(\int \Psi_e \cdot \mu \cdot \Psi_g d\tau \cdot \int \Psi_e \cdot M \cdot \Psi_g d\tau \right) \quad 1$$

K is a constant to convert the unit of molecular extinction coefficient to molecular ellipticity. c, \hbar , and N_A stand for light speed, reduced Planck constant and Avogadro's number, respectively. β is a proportionality coefficient. Ψ_e and Ψ_g are the wave functions of ground state and excited state of electrons. μ and M represent the electric field-dipole and magnetic field-dipole moment operators, respectively. $\Delta\epsilon$ is CD signal. Based on this equation, CD signal becomes larger with larger electric field-dipole interaction, i. e. larger absorption coefficient. Hence we may attribute our high CD signal to the higher absorption of our semiconducting material compared with traditional chiral organics (Fig. S31).

Conclusion

In summary, we have theoretically predicted, experimentally synthesized and comprehensively established a new low-dimensional hybrid perovskite material with both ferroelectricity and optical chirality. Structural, spectroscopy and DFT analysis have shown that the pair of synthesized material enantiomers do not have inversion symmetry. Electrical and optoelectronic transport characterizations show the existence of P-E loop, switchable and hysteresis-like pyroelectric response and a switchable photo-ferroelectric effect. Based on single crystal material, temperature dependent synchrotron X-ray diffraction, DSC, temperature dependent dielectric constant, and temperature-dependent pyroelectric current all show the existence of a ferroelectric-paraelectric phase transition at around 100 °C. CD spectroscopy and theoretical analysis demonstrate the large chirality comparable to existing chiral organics. This new class of materials will form the foundation for exploiting chirality as an additional control on the ferroelectrically-manipulated spin-orbit splitting in switchable Rashba-Dresselhaus materials (e.g. chirality-selected circular photogalvanic materials).

References

1. K. Yamauchi, P. Barone, T. Shishidou, T. Oguchi, S. Picozzi, Coupling Ferroelectricity with Spin-Valley Physics in Oxide-Based Heterostructures. *Physical review letters* **115**, 037602 (2015).
2. D. Di Sante, P. Barone, R. Bertacco, S. Picozzi, Electric control of the giant Rashba effect in bulk GeTe. *Advanced materials* **25**, 509–513 (2013).
3. S. Picozzi, Ferroelectric Rashba semiconductors as a novel class of multifunctional materials. *Frontiers in Physics* **2**, (2014).
4. D. Di Sante *et al.*, Intertwined Rashba, Dirac, and Weyl Fermions in Hexagonal Hyperferroelectrics. *Physical review letters* **117**, 076401 (2016).
5. J. He *et al.*, Tunable metal-insulator transition, Rashba effect and Weyl Fermions in a relativistic charge-ordered ferroelectric oxide. *Nature communications* **9**, 492 (2018).
6. M. Kim, J. Im, A. J. Freeman, J. Ihm, H. Jin, Switchable $S=1/2$ and $J=1/2$ Rashba bands in ferroelectric halide perovskites. *P Natl Acad Sci USA* **111**, 6900–6904 (2014).
7. F. de Juan, A. G. Grushin, T. Morimoto, J. E. Moore, Quantized circular photogalvanic effect in Weyl semimetals. *Nature communications* **8**, (2017).
8. P. Hosur, Circular photogalvanic effect on topological insulator surfaces: Berry-curvature-dependent response. *Phys Rev B* **83**, (2011).
9. K. Werner, Experimental and phenomenological aspects of circular birefringence and related properties in transparent crystals. *Reports on Progress in Physics* **63**, 1575 (2000).
10. S. Yang *et al.*, Spin-Selective Transmission in Chiral Folded Metasurfaces. *Nano Letters*, (2019).
11. R. Ogier, Y. Fang, M. Käll, M. Svedendahl, Near-Complete Photon Spin Selectivity in a Metasurface of Anisotropic Plasmonic Antennas. *Physical Review X* **5**, 041019 (2015).
12. R. Naaman, D. H. Waldeck, Spintronics and Chirality: Spin Selectivity in Electron Transport Through Chiral Molecules. *Annual Review of Physical Chemistry* **66**, 263–281 (2015).
13. M. Kettner *et al.*, Spin Filtering in Electron Transport Through Chiral Oligopeptides. *The Journal of Physical Chemistry C* **119**, 14542–14547 (2015).
14. P. Qin *et al.*, Inorganic hole conductor-based lead halide perovskite solar cells with 12.4% conversion efficiency. *Nature communications* **5**, 3834 (2014).
15. F. Hao, C. C. Stoumpos, D. H. Cao, R. P. H. Chang, M. G. Kanatzidis, Lead-free solid-state organic-inorganic halide perovskite solar cells. *Nature Photonics* **8**, 489 (2014).
16. Y. Wang *et al.*, Photon Transport in One-Dimensional Incommensurately Epitaxial CsPbX₃ Arrays. *Nano Letters* **16**, 7974–7981 (2016).
17. Z. Chen, Y. Guo, E. Wertz, J. Shi, Merits and Challenges of Ruddlesden-Popper Soft Halide Perovskites in Electro-Optics and Optoelectronics.

- Advanced materials* **31**, 1803514 (2019).
18. C. K. Yang *et al.*, The First 2D Homochiral Lead Iodide Perovskite Ferroelectrics: [R- and S-1-(4-Chlorophenyl)ethylammonium](2)PbI₄. *Advanced materials* **31**, (2019).
 19. W. Q. Liao *et al.*, A molecular perovskite solid solution with piezoelectricity stronger than lead zirconate titanate. *Science* **363**, 1206+ (2019).
 20. Y. M. You *et al.*, An organic-inorganic perovskite ferroelectric with large piezoelectric response (vol 357, pg 306, 2017). *Science* **357**, 306-309 (2017).
 21. T.-T. Sha *et al.*, Fluorinated 2D Lead Iodide Perovskite Ferroelectrics. *Advanced materials* **31**, 1901843 (2019).
 22. X.-N. Hua *et al.*, A Room-Temperature Hybrid Lead Iodide Perovskite Ferroelectric. *Journal of the American Chemical Society* **140**, 12296-12302 (2018).
 23. H.-Y. Ye *et al.*, Bandgap Engineering of Lead-Halide Perovskite-Type Ferroelectrics. *Advanced materials* **28**, 2579-2586 (2016).
 24. W.-Q. Liao *et al.*, A lead-halide perovskite molecular ferroelectric semiconductor. *Nature communications* **6**, 7338 (2015).
 25. W. Zhou *et al.*, *Lattice Dynamics and Thermal Stability of Cubic Phase CsPbI₃ Quantum Dots*. (2018), vol. 9, pp. 4915-4920.
 26. P. Pistor, A. Ruiz, A. Cabot, V. Izquierdo-Roca, Advanced Raman Spectroscopy of Methylammonium Lead Iodide: Development of a Non-destructive Characterisation Methodology. *Scientific Reports* **6**, 35973 (2016).
 27. S.-T. Ha, C. Shen, J. Zhang, Q. Xiong, Laser cooling of organic - inorganic lead halide perovskites. *Nat Photon* **10**, 115-121 (2016).
 28. J. Zhang, D. Li, R. Chen, Q. Xiong, Laser cooling of a semiconductor by 40 kelvin. *Nature* **493**, 504 (2013).
 29. S. Li, J. Luo, J. Liu, J. Tang, Self-Trapped Excitons in All-Inorganic Halide Perovskites: Fundamentals, Status, and Potential Applications. *The Journal of Physical Chemistry Letters* **10**, 1999-2007 (2019).
 30. W. J. Turner, W. E. Reese, G. D. Pettit, Exciton Absorption and Emission in InP. *Physical Review* **136**, A1467-A1470 (1964).
 31. M. Fukunaga, Y. Noda, *Improvement of the Double-wave Method for Ferroelectric Hysteresis Loops and Its Application to Multiferroic EuMn₂O₅*. (2009), vol. 55, pp. 888-892.
 32. M. Fukunaga, Y. Noda, New Technique for Measuring Ferroelectric and Antiferroelectric Hysteresis Loops. *Journal of the Physical Society of Japan* **77**, 064706 (2008).
 33. L. Hu, S. Dalgleish, M. M. Matsushita, H. Yoshikawa, K. Awaga, Storage of an electric field for photocurrent generation in ferroelectric-functionalized organic devices. *Nature communications* **5**, 3279 (2014).
 34. S. Hong *et al.*, Large Resistive Switching in Ferroelectric BiFeO₃ Nano-Island Based Switchable Diodes. *Advanced materials* **25**, 2339-2343 (2013).

35. R. Guo *et al.*, Non-volatile memory based on the ferroelectric photovoltaic effect. *Nature communications* **4**, 1990 (2013).
36. C. Ge *et al.*, Numerical investigation into the switchable diode effect in metal-ferroelectric-metal structures. *Applied Physics Letters* **99**, 063509 (2011).
37. C. Wang *et al.*, Switchable diode effect and ferroelectric resistive switching in epitaxial BiFeO₃ thin films. *Applied Physics Letters* **98**, 192901 (2011).
38. Z. Chen *et al.*, Regulating Carrier Dynamics in Single Crystal Halide Perovskite via Interface Engineering and Optical Doping. *Advanced Electronic Materials* **2**, 1600248 (2016).
39. J. P. Perdew, K. Burke, M. Ernzerhof, Generalized gradient approximation made simple. *Physical review letters* **77**, 3865-3868 (1996).
40. A. S. Sigov, M. I. Maleto, E. P. Pevtsov, V. V. Chernokozhin, Polarization, pyroelectric coefficient, and current-voltage characteristics of PZT thin films. *Ferroelectrics* **226**, 183-190 (1999).
41. H.-Y. Ye *et al.*, Metal-free three-dimensional perovskite ferroelectrics. *Science* **361**, 151-155 (2018).
42. G. Long *et al.*, Spin control in reduced-dimensional chiral perovskites. *Nature Photonics* **12**, 528-533 (2018).
43. J. Ahn *et al.*, A new class of chiral semiconductors: chiral-organic-molecule-incorporating organic-inorganic hybrid perovskites. *Materials Horizons* **4**, 851-856 (2017).
44. J. A. Schellman, Symmetry rules for optical rotation. *Accounts of Chemical Research* **1**, 144-151 (1968).
45. J. A. Schellman, Circular dichroism and optical rotation. *Chemical Reviews* **75**, 323-331 (1975).
46. A. Altomare *et al.*, SIR97: a new tool for crystal structure determination and refinement. *Journal of Applied Crystallography* **32**, 115-119 (1999).
47. G. Sheldrick, A short history of SHELX. *Acta Crystallographica Section A* **64**, 112-122 (2008).
48. R. Sundararaman *et al.*, JDFTx: Software for joint density-functional theory. *Softwarex* **6**, 278-284 (2017).
49. J. Heyd, G. E. Scuseria, M. Ernzerhof, Hybrid functionals based on a screened Coulomb potential. *The Journal of Chemical Physics* **118**, 8207-8215 (2003).
50. K. F. Garrity, J. W. Bennett, K. M. Rabe, D. Vanderbilt, Pseudopotentials for high-throughput DFT calculations. *Comp Mater Sci* **81**, 446-452 (2014).
51. S. Grimme, Semiempirical GGA-type density functional constructed with a long-range dispersion correction. *J Comput Chem* **27**, 1787-1799 (2006).

Materials and Methods

Synthesis

R-CYHEAPbI₃ / S-CYHEAPbI₃ was synthesized by solution method. Lead iodine (PbI₂, 0.25 mmol, Sigma Aldrich), R-CYHEA / S-CYHEA (1 mmol, Sigma Aldrich) and hydriodic acid aqueous solution (HI, 6 mL, ≥47.0%, Sigma-Aldrich) were mixed in a round bottom flask in silicon oil bath. The flask was heated to 150 °C for 2 h with refluxing. Excess R-CYHEA / S-CYHEA and HI were used deliberately to advance the reaction and make sure PbI₂ was completely consumed, and can be removed after the reaction by filtration. After the heating process, a clear solution was obtained and by slowly decreasing the temperature to room temperature at 0.1 °C/min, large needle-like single crystals were successfully synthesized.

Chemical vapor deposition (CVD) method was also used to synthesize this material. We used a home-made CVD system (Extech 48VFL13 PID controller). Mica (SPI Grade V-5) was used as substrate. The temperature at the furnace center was around 400 °C, where one of the precursors PbI₂ was placed. The other precursor, (R)-(-)-1-Cyclohexylethan-1-aminium iodide / (S)-(+)-1-Cyclohexylethan-1-aminium iodide (R-CYHEAI / S-CYHEAI), which was prepared by mixing R-CYHEA / S-CYHEA and HI in ice water bath, was placed in upstream position, 2 inches away from the zone center, while substrates was placed at downstream position. The system was pumped to 0.5 Torr before the deposition, after which the base pressure was maintained to be around 200 Torr with a 200 sccm flow of argon. After 30min's growth, we successfully got some needle-like crystals on the substrate.

Thin films preparation

Thin films were prepared by spin coating method (Headway manual spin coater). R-CYHEAPbI₃ / S-CYHEAPbI₃ was dissolved in acetone, then saturated solution was spin coated on silicon wafers (si, n-type, $1.0 - 1.3 \times 10^{15}$ 1/cm³ phosphor doped, Silicon Valley Microelectronics), fluorine doped tin oxide coated glasses (FTO, ~7 Ω/sq, Sigma Aldrich), freshly cleaved sodium chloride substrates (NaCl, Ted Pella), freshly cleaved potassium chloride substrates (KCl, Ted Pella), quartz slides (TGP) and glass slides (VWR) at 2000, 4000, 6000, 8000, and 10000 rpm for 30 s. After the spin coating process, high quality films were easily prepared and annealing was not required.

Devices preparation

For electrical measurements, 40 nm thick round gold electrodes with a diameter of around 1 mm was deposited on the thin films by e-beam deposition method to form

usable devices with Tesmescal e-beam evaporator. Those devices were used for P-E loop tests and photo response tests.

Our single crystal device is prepared with a submillimeter size single crystal sample between two piles of silver paste on a glass substrate, forming a lateral device. This device was used for temperature dependent dielectric constant measurement and pyroelectric tests (Fig. S25).

NMR and FTIR measurement

Our material was dissolved in Dimethyl Sulfoxide-d₆ (DMSO-d₆) for NMR measurement with 500MHz Agilent NMR Spectrometer. Thin film on NaCl was used for FTIR measurement with Perkin Elmer Spectrum One FT-IR spectrometer.

Optical measurements

Optical images and transmission of linear polarized white light were measured with our Nikon Ti-S optical microscope. Thin films on KCl were used for Raman spectrum measurement with Witec Alpha 300 confocal Raman microscope and a 532 nm continuous wave (CW) laser. PL measurement was done at room temperature with a home-built PL system (Thorlabs 4 Megapixel Monochrome Scientific CCD Camera, Princeton Instruments SP-2358 spectrograph, Nikon Ti-S optical microscope and Picoquant 405nm pulsed laser). Transmission spectrum was measured using thin film on NaCl with a USB4000-UV-VIS spectrometer. The photo response of this material was measured with a home-made system (Autolab PGSTAT302N potentiostat, Thorlabs Compact Laser Diode Module with Shutter, 405/635 nm, 4.0 mW). Devices on FTO was used in these measurements. SHG measurement was performed with a home-made system (Keopsys KPS-BT2-YFL-1083-40-COL 1083 nm 3 W CW fiber laser, Thorlabs 4 Megapixel Monochrome Scientific CCD Camera, Princeton Instruments SP-2358 spectrograph, and Nikon Ti-S optical microscope). TD SHG was performed with Linkam Scientific Instrument TMS94 temperature controller.

XRD measurements

Powder XRD was performed using Cu K α radiation on a Bruker D8 Focus diffractometer with a LynxEye detector. Rietveld refinements were performed in TOPAS (Bruker AXS). Single-crystal XRD experiments were carried out by mounting needle-like crystals on a loop with a tiny amount of Paratone-N oil (T = -163 (2) °C) or epoxy (T = 25 °C). All reflection intensities were measured using a SuperNova

diffractometer (equipped with an Atlas detector) with Mo K α radiation ($\lambda = 0.71073 \text{ \AA}$) under the CrysAlisPro software suite (version 1.171.36.28, Agilent Technologies, 2012). CrysAlisPro was also used to index the cell dimensions and to perform data reduction. The generation of the initial models and subsequent structure refinements were conducted using SIR97(46) and SHELXL-20132(47), respectively. After the refinement of all of the atomic positions, the collected data were corrected for absorption (i.e., a face-indexed analytical absorption correction was applied using CrysAlisPro). The displacement parameters were then refined as anisotropic and weighting schemes were applied during the final stages of refinement.

Temperature dependent synchrotron X-ray diffraction results was recorded from 0 °C up to 175 °C in 5 °C for each step with X-ray wavelength of 0.1173 Å, and Cryostream 700 to control temperature. For each temperature point, the single long shot image is the cumulative collection of the single crystal diffraction as a function of rotation along the crystallographic zone axis of the long side of the small single crystal (Fig. S12), which should be the [010] direction.

EBSD measurements

EBSD measurements were performed with Oxford AZTEC system on our needle-like single crystals.

Electrical properties measurements

PE loop measurements were performed with a home-built double wave method system (BK Precision 2190D oscilloscope, AFG1062 Tektronix Arbitrary Waveform Generator) at different frequency. Detailed information about double wave method can be found in SI (Fig. S24).

Switchable diode effect was measured with a home-built system consisting of Autolab PGSTAT302N potentiostat and radio shack 10 mm blue LED lamp (465nm to 467.5nm).

Temperature dependence of dielectric constant was measured with a home-built system (AFG1062 Tektronix Arbitrary Waveform Generator, BK Precision 2190D oscilloscope, Falco Systems WMA-02 amplifier) and temperature was controlled by a cyrostage (Linkam Scientific Instrument, TMS94). Impedance was measured and then dielectric constant was calculated:

$$\varepsilon' = \frac{d}{2\pi f S \varepsilon_0} \frac{Z''}{Z'^2 + Z''^2} \quad 2$$

ε' is real part of dielectric constant ($\varepsilon = \varepsilon' - i\varepsilon''$), d is distance between two electrodes, S is device area, f is frequency of applied sine wave, ε_0 is vacuum permittivity, Z is impedance ($Z = Z' + Z''$).

Pyroelectric current was measured with a potentiostat (Autolab PGSTAT302N) and a cyrostage (Linkam Scientific Instrument, TMS94). Similar to P-E loop measurements, pyroelectric coefficient vs. poling electric field loop was obtained by poling our device at a series of voltage: 2000 V, 1000 V, 500 V, 0 V, -500 V, -1000 V, -2000 V, -1000 V, -500 V, 0 V, 500 V, 1000 V, and 2000 V, and measured the pyroelectric coefficient after each poling. Temperature dependence of pyroelectric current was measured with a ramp speed of 10 °C/min.

DSC measurements

DSC was measured with a differential scanning calorimeter (TA Instruments, DSC-Q100) under nitrogen atmosphere. Temperature range was set to be 20 °C to 120 °C with a ramp speed of 10 °C/min.

CD measurements

CD was performed on Jasco 815 CD spectrometer.

DFT calculations

We perform Density-functional theory calculations using the open-source plane-wave software; JDFTx (48) with the Heyd-Scuseria-Ernzerhof (HSE06) (49) exchange-correlation functional, ultrasoft pseudopotentials (50) and a kinetic energy cutoff of 20 Hartrees for wavefunctions and 100 Hartrees for the charge density. We employ DFT+D2 (51) pair-potential corrections for the Van der Waals interaction and integrate over the Brillouin zone using a $2 \times 2 \times 1$ Γ -centered k-point mesh. The band structure is then calculated on a high-symmetry k-point path using maximally localized wannier functions.

Supplementary materials:

- (1) Structural characterization: Table S1-S3, Figure S1-S17, Video 1-2
- (2) Optical characterization: Figure S18-S23
- (3) Ferroelectricity and pyroelectricity: Figure S24-S28
- (4) Photo Ferroelectricity: Figures S29-S30

(5) Chirality: Figures S31-S32

Acknowledgements: JS and RS acknowledges start-up funding from the Department of Materials Science and Engineering at Rensselaer Polytechnic Institute, NSF awards under No. 1635520, No. 1712752, the Air Force Office of Scientific Research under award number FA9550-18-1-0116, the Office of Naval Research under award number N000141812408. Calculations were performed at the Center for Computational Innovations at Rensselaer Polytechnic Institute. This research used resources of the Advanced Photon Source, a U.S. Department of Energy (DOE) Office of Science User Facility operated for the DOE Office of Science by Argonne National Laboratory under Contract No. DE-AC02-06CH11357. This material is partially based upon work supported by the NSF-MIP Platform for the Accelerated Realization, Analysis, and Discovery of Interface Materials (PARADIM) under Cooperative Agreement No. DMR-1539918.

Author contributions: Y.H. and Z.C. grew the materials fabricated the films. Y.H., Z.C. and J.J. conducted the electrical and optoelectrical transport studies. F.F. and R.S. conducted computational simulations. H. Z. and Y.R. conducted and analyzed temperature-dependent Synchrotron XRD. W.A.P. and M.A.S. conducted and analyzed single crystal XRD. Z.Z. and E.F.P. conducted and analyzed DSC and NMR results. Y.H., Y.G., R.H., J.J., L.Z. and Y.W. conducted device fabrication. Y.H. and Y.G. conducted and analyzed CD spectra. B.W. and D.G. conducted FTIR study and helped on XRD study. Y.H. and J.J. conducted and analyzed SHG. L.Z. conducted and analyzed AFM and SEM studies. Z.L. and X.S. conducted EBSD study. X.S. conducted PVD growth. Y.H. and F.F. wrote the manuscript. T.M.L., E.W., R.S., J.F. and J.S. all participated in the analysis of data and revision of the manuscript. J.S. and R.S. conceived and supervised the project.

Competing interests: The authors declare that they have no competing interests. **Data and materials availability:** All data needed to evaluate the conclusions in the paper are present in the paper and/or the Supplementary Materials. Additional data related to this paper may be requested from the authors.

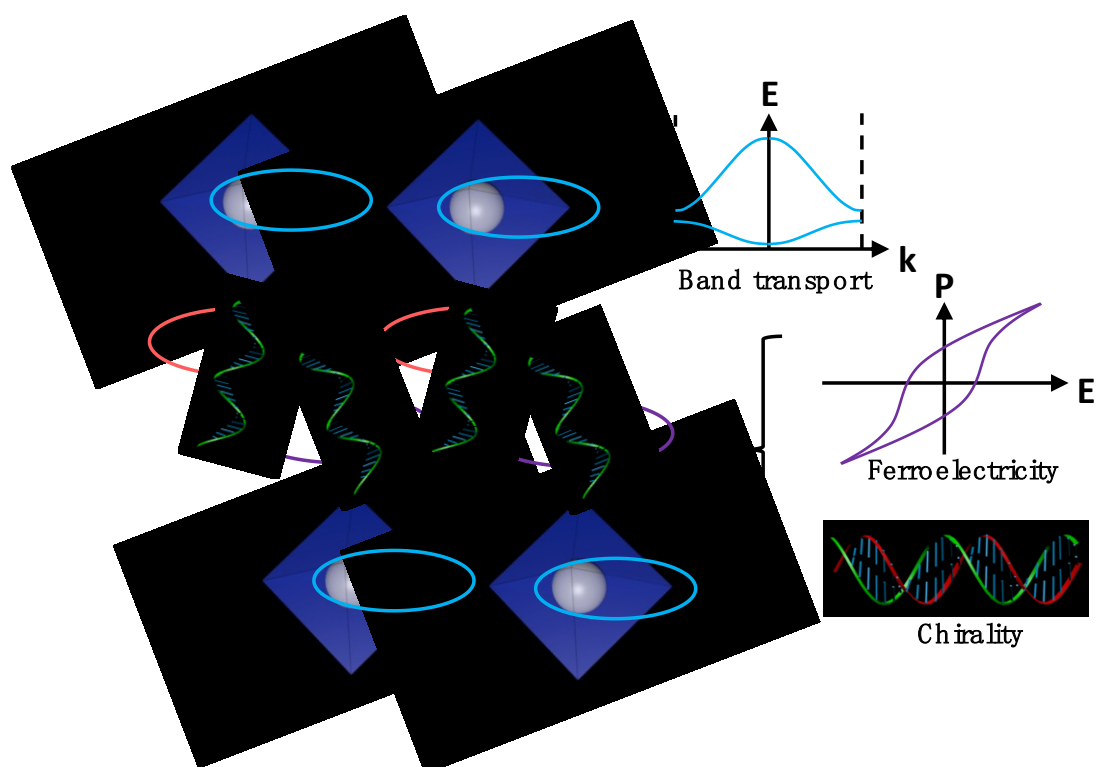


Fig. 1 Design principle. Lead-halogen octahedra controls the semiconducting property independently from the organic molecule that can be engineered to introduce new properties, such as simultaneous ferroelectricity and chirality achieved here.

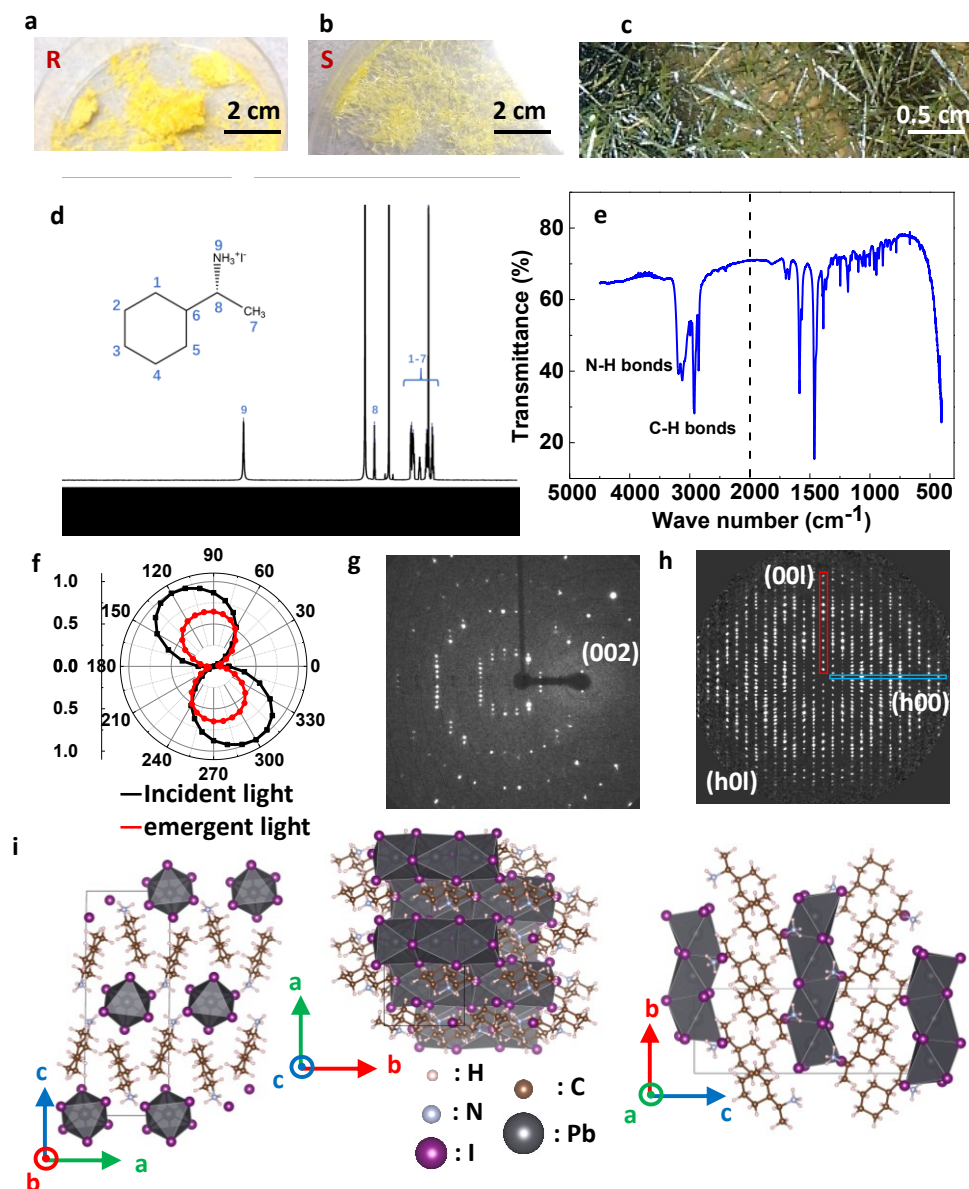


Fig. 2 Structure determination. **a-b**, Optical images of our materials prepared with a pair of enantiomers, R-CYHEAI and S-CYHEAL, with **c**, needle-like crystals. (Photo Credit for **a**, **b** and **c**: Yang Hu, Rensselaer Polytechnic Institute). **d**, NMR results of our material (synthesized with R-CYHEA) dissolved in DMSO- d_6 . **e**, FTIR result of our material (synthesized with S-CYHEA). N-H bond peaks shows up at around 3200 cm^{-1} , which is a little bit away from that of S-CYHEA, but is almost the same as that of S-CYHEAI indicating this shift comes from the formation of $-\text{NH}_3^+$. **f**, Transmission spectrum with polarized light. The rotation of polarization direction indicates the existence of a single fast axis and the good single crystal quality. **g**, Single crystal XRD diffraction pattern of our needle-like single crystal at -173°C . **h**, Corresponding

digitally reconstructed precession photograph of our crystal at 25 °C, showing the (h0l) planes. **i**, Schematic drawing of the structure of our 1-D perovskite, where lead, iodine, carbon, nitrogen, and hydrogen atoms are represented by black, purple, brown, blue, and white spheres, respectively.

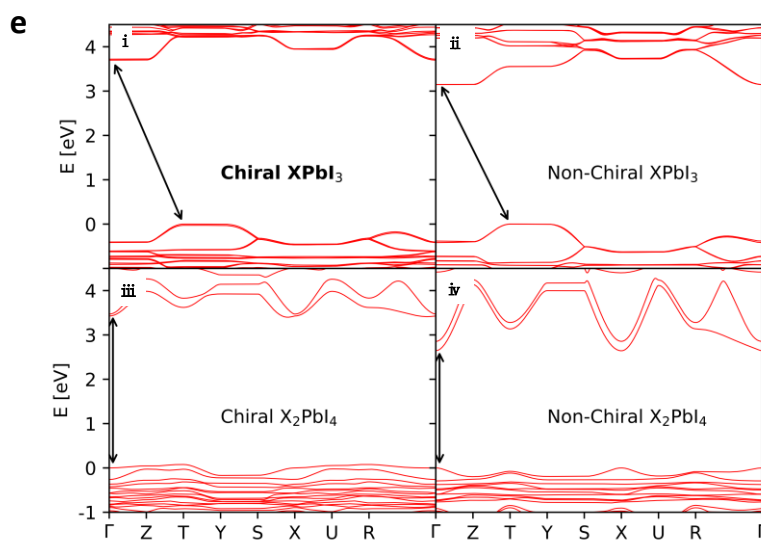
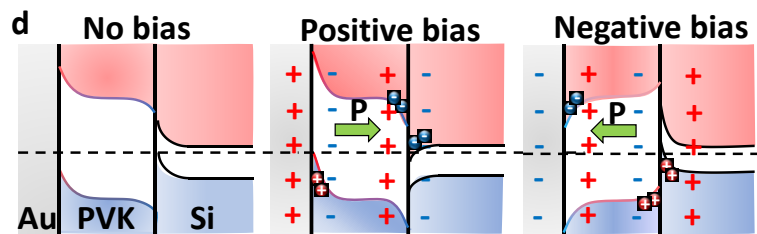
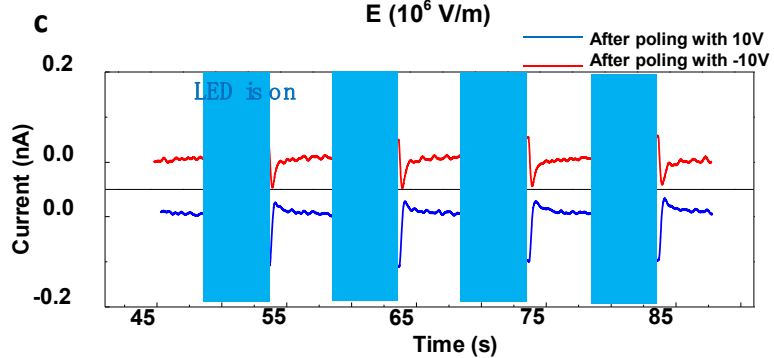
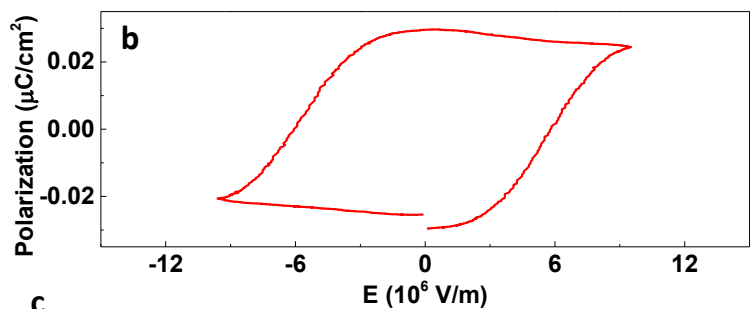
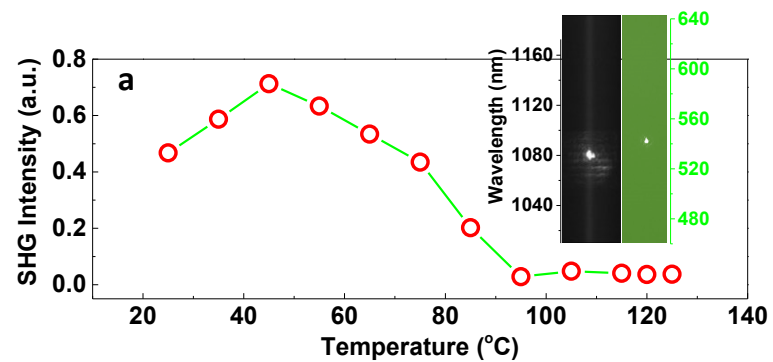


Fig. 3 Switchable photovoltaic ferroelectric effect. **a**, Temperature-dependent Second harmonic generation (SHG) reveals a transition from an inversion-symmetry-broken to an inversion-symmetric phase at 85 °C. Inset: SHG peak at 540 nm from a 1080 nm infrared laser. **b**, Polarization-Electric field (PE) loop of our perovskite confirming its ferroelectricity. Test was done at 800 Hz. **c**, Switchable diode effect: After poling with +10 V and -10 V for 200 s, photo current without bias is negative and positive respectively, because of **d**, Band structure of our polycrystal device under zero bias, positive bias, and negative bias, respectively. A reversal in the band-bending and resulting diode orientations are shown in the device. **e**, Electronic band structure for chiral CYHEA (**i**, **iii**) and non-chiral CYHEA (**ii**, **iv**) XPbI_3 (**i**, **ii**) and X_2PbI_4 (**iii**, **iv**) stoichiometries. Band gaps increase and switch from direct to indirect on going from X_2PbI_4 to XPbI_3 for each material: from 3.43 eV to 3.70 eV for the chiral material, and from 2.64 eV to 3.15 eV for the non-chiral one.

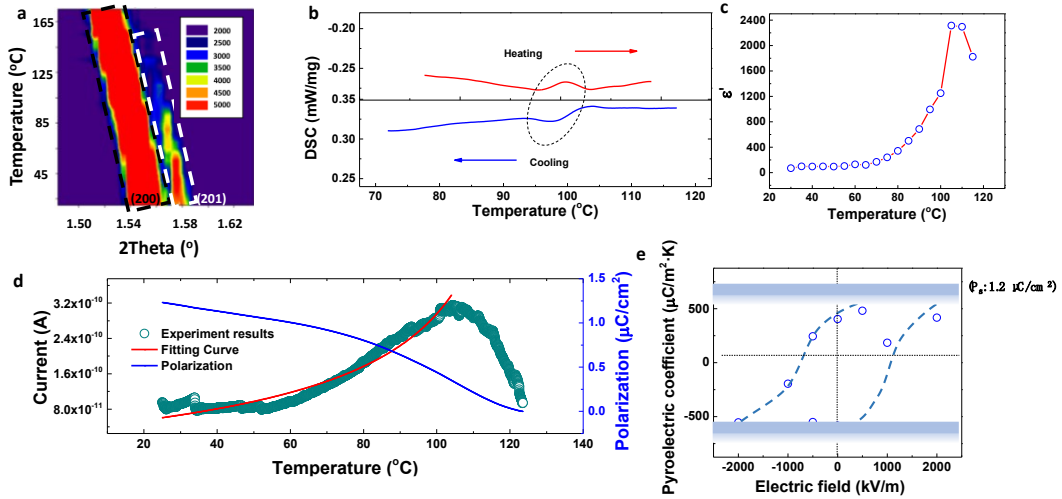


Fig. 4 Single crystal phase transition and pyroelectric study. **a**, Temperature dependent synchrotron X-ray diffraction results. Intensity of peak (201) decreases dramatically, which indicates a phase transition at around 100 °C. More detailed results can be found in our SI and supplementary videos. **b**, DSC results. Sudden increase and decrease indicate a phase transition at around 100 °C. **c**, Temperature dependence of real part of dielectric constant. A peak at around 100 °C indicates a phase transition. **d**, Temperature dependence of pyroelectric current. The red curve and blue curve are fitting to Landau theory and polarization vs. temperature curve obtained by integration, respectively. The peak at around 100 °C indicates a phase transition. Our experiment results fit well with Landau theory, and the polarization at room temperature is around 1.2 $\mu\text{C}/\text{cm}^2$ based on integration. **e**, Pyroelectric coefficient vs. poling electric field loop. Dash line is a trend line showing a hysteresis.

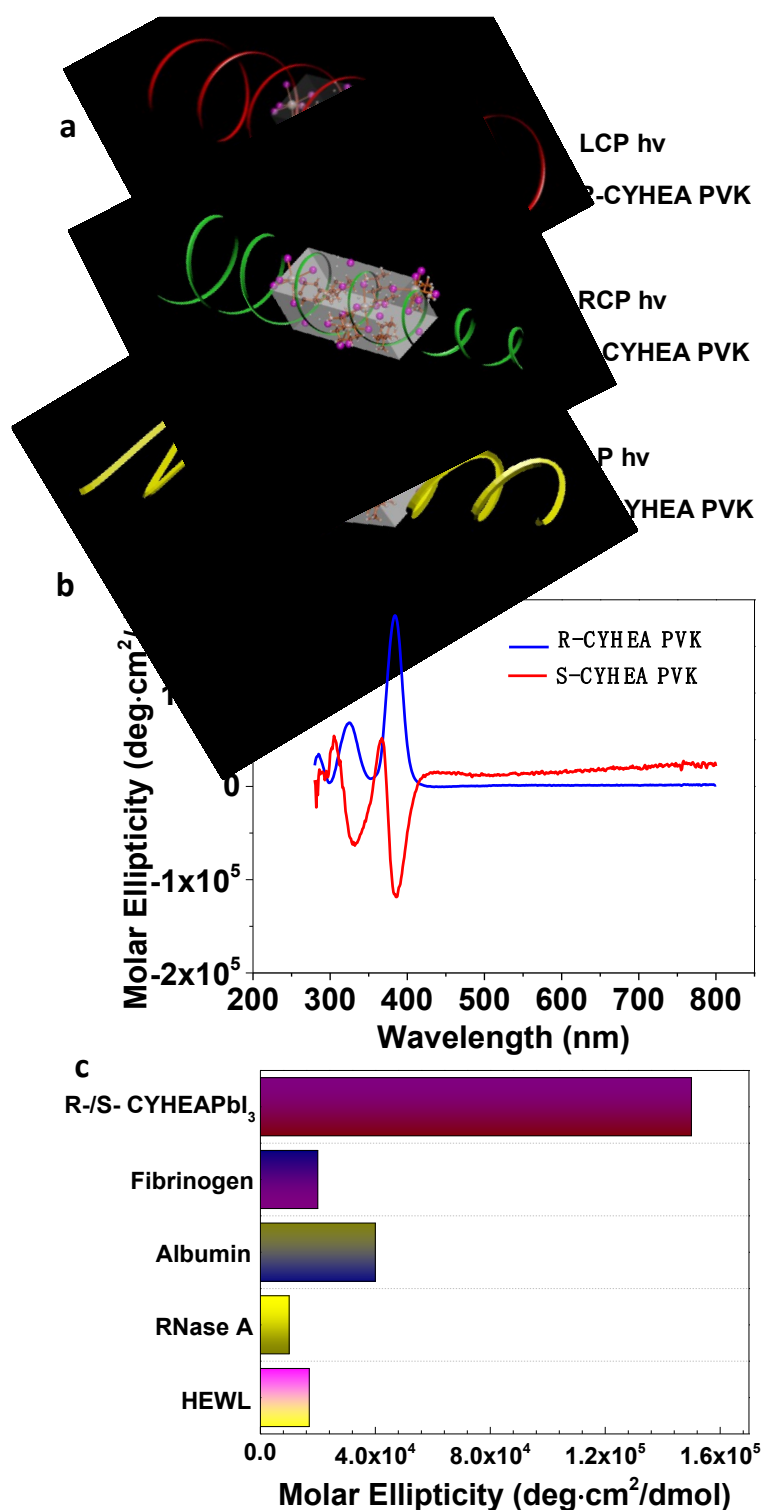


Fig. 5 Chirality. **a**, Schematic of Circular Dichroism (CD) measurements: chiral material absorbs different amount of left- and right- circular polarized light, changing linear polarization to elliptical. **b**, CD spectrum of the synthesized crystals show opposite signals at the same position indicating that they are enantiomers. **c**, Our new

chiral ferroelectric material surpasses the CD signals of conventional chiral materials.